International Journal of Mechanical Sciences 205 (2021) 106591

Contents lists available at ScienceDirect

International Journal of Mechanical Sciences

journal homepage: www.elsevier.com/locate/ijmecsci

Characteristic and mechanism of crack initiation and early growth of an additively manufactured Ti-6Al-4V in very high cycle fatigue regime

Chengqi Sun [a,b,*], Weiqian Chi [c], Wenjing Wang [c], Yan Duan [d]

[a] State Key Laboratory of Nonlinear Mechanics, Institute of Mechanics, Chinese Academy of Sciences, Beijing 100190, China
[b] School of Engineering Science, University of Chinese Academy of Sciences, Beijing 100049, China
[c] School of Mechanical, Electronic and Control Engineering, Beijing Jiaotong University, Beijing 100044, China
[d] Xi'an Bright Laser Technologies Co., Ltd., Xi'an 710117, China

A R T I C L E I N F O

Keywords:
Very high cycle fatigue
Additively manufactured Ti-6Al-4V
Selective laser melting
Crack initiation mechanism
Grain refinement

A B S T R A C T

In this paper, very high cycle fatigue (VHCF) behavior of an additively manufactured (AM) Ti-6Al-4V by selective laser melting process and post-heat treated by hot-isostatic pressing is investigated by ultrasonic frequency fatigue test and rotating bending fatigue test. It is shown that the fatigue crack initiation is related to loading types in VHCF regime. Under rotating bending fatigue test, the fatigue crack initiates from specimen surface. While for ultrasonic frequency fatigue test, both the surface and the interior crack initiations are observed. For interior crack initiation, the fracture surface presents fish-eye like pattern and fine granular area (FGA) morphology. Electron backscatter diffraction and transmission electron microscopy observations indicate that there are discontinuous refined grain regions beneath the fracture surface in crack initiation and early growth region (i.e. FGA). It is proposed that the mechanism of crack initiation and early growth of titanium alloys in VHCF regime is attributed to the grain refinement caused by dislocation interaction over a number of cyclic loadings followed by cracks combined with the cracks formed at defects, α-phase, interfaces, etc. during cyclic loadings. The paper also indicates that the fatigue performance of the present AM Ti-6Al-4V is comparable to that of the conventionally processed Ti-6Al-4V.

1. Introduction

Additive manufacturing, as a novel technology, has great prospect for the production of small lot sizes or the component parts with complex geometries and structures due to its digital process and layer manufacturing principle. By using the additive manufacturing technology, many metallic materials could be manufactured [1,2], such as Ti-6Al-4V [3-5], AISI 420 stainless steel [6], Inconel 718 [7], and so on.

Titanium alloys have been widely used in the aerospace and biomedical industries due to their high strength, low density and high temperature resistance, which might be also for the additively manufactured (AM) titanium alloys [8-11]. In potential use of the AM titanium alloys, some of the component parts inevitably subject to fatigue loadings during service. For example, the turbine blade of aircraft engines needs to endure more than 10^9 cyclic loadings in service [12]. However, the process inherent surface roughness and defects (e.g. gas porosity, lack of fusion) due to the manufacturing process generally lower the fatigue strength of AM titanium alloys compared to the conventionally wrought titanium alloys [13-15]. Especially, numerous studies in recent decades have shown that the conventionally processed (CP) titanium alloys exhibit no traditional fatigue limit defined at 10^7 cycles, i.e. the failure of titanium alloys occurs in very high cycle fatigue (VHCF) regime [16-19]. The demand of high safety and reliability requires the fully understanding of the VHCF behavior of AM titanium alloys.

As far as the authors' knowledge, there are only a few studies on VHCF behavior of AM titanium alloys [20,21]. The existing results indicate that the fatigue crack of AM Ti-6Al-4V in non-hot-isostatic-pressing condition initiates from the defects (such as gas porosity and lack of fusion) produced during the manufacturing process [11,22,23]. While for the hot-isostatic-pressed AM Ti-6Al-4V, the fatigue crack initiates at α-phase or α-phase clusters [23]. Especially, the fracture surface of interior crack initiation presents the fish-eye pattern and the fine granular area (FGA) feature [11,20,23], similar to that observed for CP titanium alloys in VHCF regime [24,25]. It has been shown that the crack initiation and early growth (i.e. FGA) consumes most of the total fatigue life, and exhibits a layer of nano-grains for VHCF behavior of CP Ti-6Al-4V at the stress ratio R =–1 [24]. So, it is very essential to explore the mechanism of crack initiation and early growth for AM titanium alloys. What is the microstructure characteristic of FGA for AM titanium alloys? What is the evolutionary process of the fatigue crack in FGA? These issues have remained to be elucidated.

* Corresponding author.
E-mail address: scq@lnm.imech.ac.cn (C. Sun).

https://doi.org/10.1016/j.ijmecsci.2021.106591
Received 20 March 2021; Received in revised form 8 June 2021; Accepted 9 June 2021
Available online 16 June 2021
0020-7403/

In this paper, the ultrasonic frequency fatigue test (f=20 kHz) and the rotating bending fatigue test (f=50 Hz) are performed on the specimens of an AM Ti-6Al-4V manufactured by the selective laser melting and post-treated by hot-isostatic pressing. The microstructure characteristic in the crack initiation and early growth region is investigated for VHCF behavior of the AM Ti-6Al-4V by using the scanning electron microscope (SEM), transmission electron microscopy (TEM) and the electron backscatter diffraction (EBSD). It is found that there is local grain refinement feature in the FGA region. Based on the observed results, the mechanism of the crack initiation and early growth for titanium alloys is discussed. Also, the effect of loading type on the fatigue behavior of the present AM Ti-6Al-4V is investigated, and its fatigue performance is compared to that of the CP Ti-6Al-4V in literature.

2. Materials and methods

2.1. Materials

The material used in this paper is an AM Ti-6Al-4V made by the selective laser melting technology on a BLT-S310 machine. The laser power is 360 W, the scanning speed is 1200 mm/s, the scanning distance is 0.1 mm, and the thickness of powder layer is 0.06 mm. The bars with the length of 100 mm and diameter 12 mm are at first produced, and then heat treated at 710°C for 2 hours in vacuum, and cooled in argon atmosphere, and finally treated by hot-isostatic pressing at 920°C and 1000 bar for 2 hours in argon atmosphere. The building direction is vertical (i.e. 90°). The chemical compositions (wt.%) of the powder are 5.97 Al, 3.93 V, 0.12 Fe, 0.015 C, 0.088 O, 0.0031 H and Ti balance. The particle size is in the range of 20-53 μm in diameter. The average of the tensile strength and the yield strength of the material are 984 MPa and 878 MPa, respectively, which are obtained by two specimens with diameter of 5 mm in test section. The microstructure of the present AM Ti-6Al-4V is basketweave. The α-lamella thickness is about 1 to 6 microns. The microstructure parallel to the building direction is shown in Fig. 1a and b.

2.2. Fatigue tests

Two different loading types are used in this paper. One is performed on an ultrasonic fatigue test system (f=20 kHz) with continuous fatigue loading, and the other is performed on a cantilever-type rotating bending machine (f=50 Hz). For ultrasonic frequency fatigue test, the resonant frequency of the specimen must be in the range of 20±0.5 kHz. The resonant frequency will decrease due to the fatigue crack initiation and growth. Once it is lower than 19.5 kHz, the resonance stops, i.e. the fatigue test terminates. The fatigue loading for ultrasonic frequency fatigue test is controlled by the displacement at the specimen end, and the applied stresses at the smallest section of the specimen are transformed to the displacement by the theoretical formula before the fatigue test. For rotating bending fatigue test, the loading is applied through suspending the weight at the outer end of the specimen by means of a helical spring. The count of the loading cycles will stop when the specimen fractures, i.e. the fatigue test terminates. Both the fatigue tests are at room temperature in air, and the stress ratio R is –1. The specimens for ultrasonic frequency fatigue test and rotating bending fatigue test are shown in Figs. 1c and 1d, respectively. For ultrasonic frequency fatigue test, the cool air is used to reduce the temperature of the specimen during the fatigue test. The tested surfaces of the specimens are all ground and polished in order to eliminate the machining scratches before fatigue test.

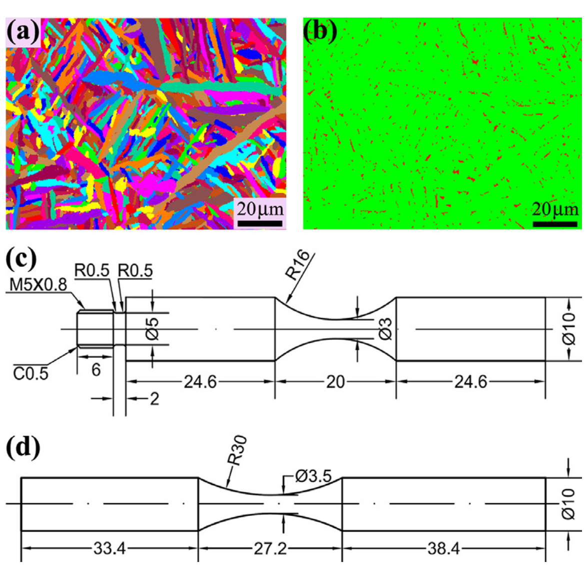

Fig. 1. Microstructure and specimen of the AM Ti-6Al-4V. (a) Microstructure; (b) Phase distribution, green color: alpha phase, red color: beta phase; (c) Specimen geometry for ultrasonic frequency fatigue test (in mm); (d) Specimen geometry for rotating bending fatigue test (in mm).

2.3. Observation and characterization

The fracture surfaces of the failed specimens are observed by a scanning electron microscope (SEM). In order to observe the microstructure characteristics beneath the fracture surface in the crack initiation and early growth region, four cross-section samples along the loading direction are prepared for the fracture surface by the focused ion beam (FIB) technique on the commercial crossbeam 540 FIB-SEM system, and then observed by the electron backscatter diffraction (EBSD) technique on the Oxford Instruments. The fracture surface of the extracted samples is protected by a coating layer of platinum during the cutting process. The microstructures of two extracted cross-section samples are also observed by the transmission electron microscopy (TEM) with the diameter of the selected area diffraction (SAD) 170 nm on the JEOL 2100F in order to further identify the microstructure characteristics beneath the fracture surface.

3. Results

3.1. Fatigue performance under ultrasonic frequency fatigue test

Fig. 2 shows the S-N data of the present AM Ti-6Al-4V under ultrasonic frequency fatigue test. It is seen from Fig. 2 that the fatigue failure of the AM Ti-6Al-4V occurs in VHCF regime, and the fatigue life increases with decreasing the stress amplitude in high cycle and VHCF regimes. The fatigue performance of the present AM Ti-6Al-4V is also compared with that of the CP Ti-6Al-4V under ultrasonic frequency fatigue test at R=–1 in literature [16,26,27] in Fig. 2. The tensile strength and yield strength of the CP Ti-6Al-4V are given in Table 1. It is seen from Fig. 2 that the fatigue performance of the present AM Ti-6Al-4V is comparable to the CP Ti-6Al-4V, and is better than the fatigue performance of the CP Ti-6Al-4V with similar basketweave microstructure.

Table 1
Tensile strength and yield strength of the CP Ti-6Al-4V in Fig. 2.

Microstructure	Tensile strength (MPa)	Yield strength (MPa)
Basketweave [16]	970	907
Bimodal [16]	967	930
Bimodal [26]	945	812
$\alpha+\beta$ [27]	1010	920

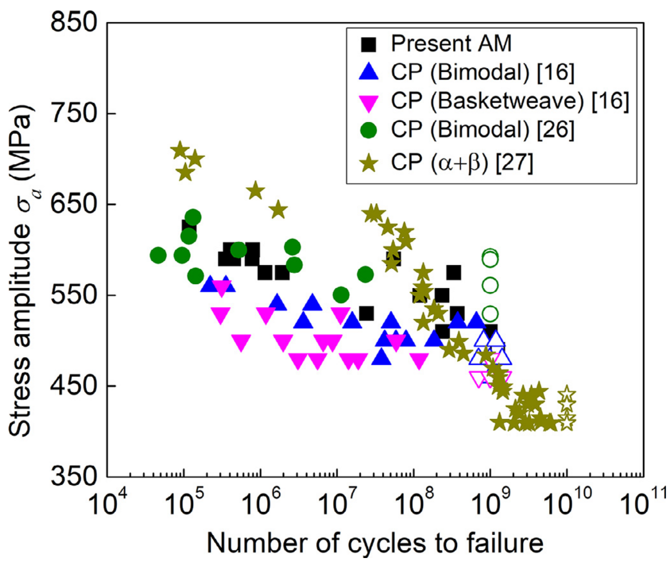

Fig. 2. Comparison of S-N data for the present AM Ti-6Al-4V with the CP Ti-6Al-4V in literature, in which the hollow symbols denote the specimens not broken at the tested loading cycles.

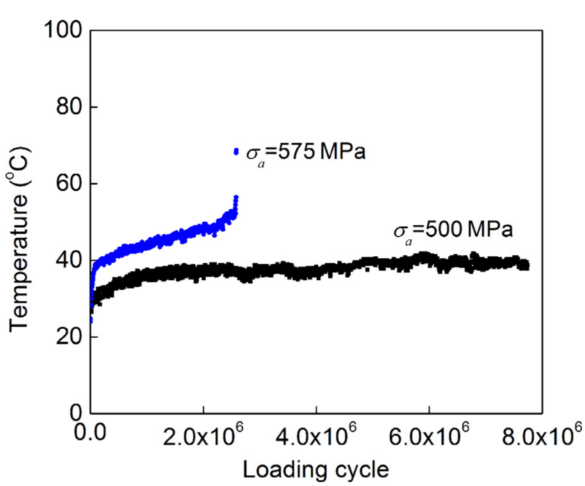

Fig. 3. Variation of surface temperature of specimens with loading cycle during ultrasonic frequency fatigue test.

3.2. Measurement of temperature under ultrasonic frequency fatigue test

Here, the surface temperature of specimens is measured through a thermocouple adhered to the surface of the small section of the specimen by the high-temperature adhesive during the ultrasonic frequency fatigue test, as that used in Ref. [18]. Fig. 3 shows the variation of the surface temperature of the smallest section with the loading cycle during ultrasonic frequency fatigue test. It is seen that the surface temperature of the specimen is related to the stress amplitude. At the stress amplitude σ_a=500 MPa, the temperature stabilizes rapidly and the stable temperature is a little higher than the room temperature. At the stress amplitude σ_a=575 MPa, the temperature increases with the loading cycle and increases sharply just before the resonance stops. It is noted that the temperature measurement is stopped after a few minutes of the stable temperature for the specimen tested at the stress amplitude σ_a=500 MPa.

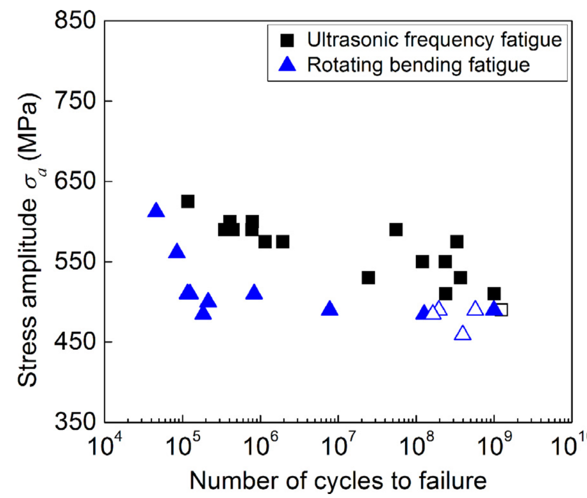

Fig. 4. Comparison of S-N data for the present AM Ti-6Al-4V under different loading types, in which the hollow symbols denote the specimens not broken at the tested loading cycles.

3.3. Fatigue performance under rotating bending fatigue test

Fig. 4 shows the fatigue performance of the present AM Ti-6Al-4V under rotating bending fatigue test, which is also compared with that under ultrasonic frequency fatigue test. Here, the local stress amplitude of the smallest section of the specimen is used for rotating bending fatigue test. It is seen that the fatigue performance of the present AM Ti-6Al-4V under ultrasonic frequency fatigue test is higher than that under rotating bending fatigue test.

3.4. SEM observation of fracture surface under ultrasonic frequency fatigue test

SEM observation indicates that the present AM Ti-6Al-4V under ultrasonic frequency fatigue test fails from the surface or the interior of the specimen in VHCF regime. For the surface induced failure mode, the fatigue crack initiates from the α grains, as shown in A-1 in Fig. 5. For the interior induced failure mode, the fracture surface presents the fish-eye like pattern and the clear FGA morphology (B-2 and C-2) or FGA like morphology (D-2 in Fig. 5). The clear FGA morphology and FGA like morphology indicate that the formation of FGA is related to the local microstructure in the crack initiation and early growth region. Similar to the VHCF behavior of hot-isostatic-pressed AM Ti-6Al-4V in literature [22,23], no crack initiation at defects such as gas porosity and lack of fusion is observed for both the surface and interior induced failure modes. The loading information, crack initiation site and FGA size for the tested specimens are shown in Table 2, in which the FGA size is taken as the positive square root of the FGA area [28]. Table 2 indicates that the fatigue crack tends to initiate from the interior of the specimen for the present AM Ti-6Al-4V under ultrasonic frequency fatigue test. It is noted that the charring characteristics are also observed for the surfaces of some failed specimens due to the final abrupt raise of temperature just before the resonance stops. For these specimens, the fracture surfaces are not observed.

3.5. SEM observation of fracture surface under rotating bending fatigue test

Fig. 6 shows the fracture surface morphology of several failed specimens under rotating bending fatigue test. Similar to the specimens under ultrasonic frequency fatigue test, no crack initiation at the defects such as gas porosity and lack of fusion is observed for specimens under rotating bending fatigue test. However, the fatigue cracks initiate from the

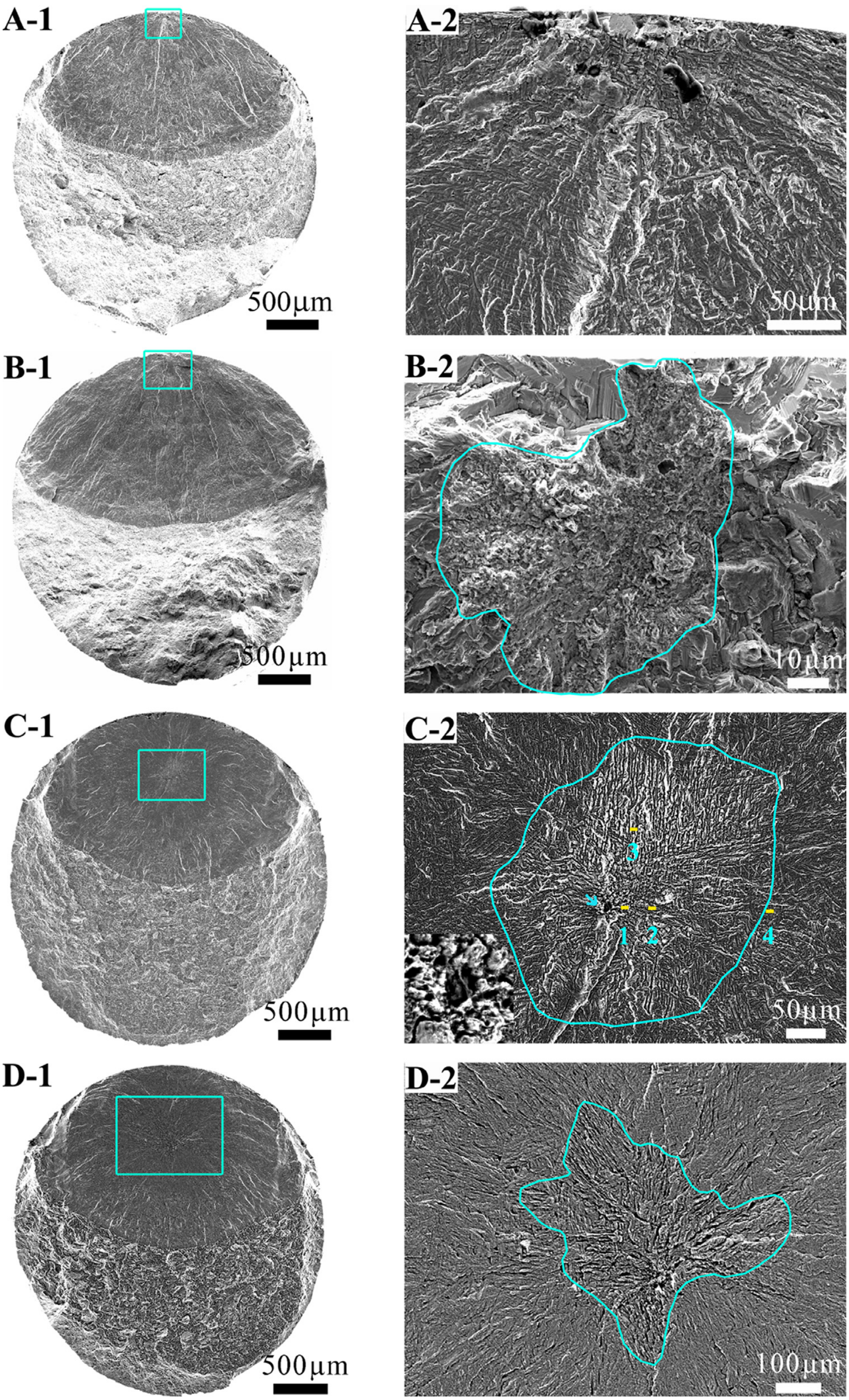

Fig. 5. Fracture surface morphology of several failed specimens under ultrasonic frequency fatigue test. A-1 and A-2: Specimen 4; B-1 and B-2: Specimen 12; C-1 and C-2: Specimen 11; D-1 and D-2: Specimen 15. A-2, B-2, C-2 and D-2 are close-ups of the rectangle regions in A-1, B-1, C-1 and D-1, respectively. The short lines in C-2 denote the locations where the samples along the loading direction for the TEM and EBSD observation are extracted. The small figure in the lower left quarter in C-2 is close-up of the region pointed by the arrow.

specimen surface for all the failed specimens under rotating bending fatigue test, which is different from those under ultrasonic frequency fatigue test. The facet feature in the crack initiation region is observed for the present AM Ti-6Al-4V under rotating bending fatigue test (B-2 in Fig. 6), similar to that observed for the fatigue of CP titanium alloys [29-32].

4. Discussion

4.1. Stress intensity factor range for FGA

The fish-eye pattern and FGA morphology are typical characteristics in the fracture surface for VHCF of high strength steels. It has been

Table 2
Loading information, crack initiation site and FGA size for the specimens under ultrasonic frequency fatigue test.

Specimen No.	Stress amplitude σ_a /MPa	Stress ratio R	Cycles	Crack initiation site	FGA size a_{FGA}/μm
1	625	−1	1.18×10^5	–	
2	600	−1	4.07×10^5	–	
3	600	−1	7.91×10^5	–	
4	590	−1	5.51×10^7	Surface	
5	590	−1	7.83×10^5	–	
6	590	−1	3.50×10^5	–	
7	590	−1	4.48×10^5	–	
8	575	−1	3.34×10^8	Interior	248.1
9	575	−1	1.93×10^6	–	
10	575	−1	1.15×10^6	–	
11	550	−1	1.21×10^8	Interior	314.7
12	550	−1	2.35×10^8	Interior	62.2
13	530	−1	3.71×10^8	Interior	86.5
14	530	−1	2.43×10^7	–	
15	510	−1	1.00×10^9	Interior	391.9
16	510	−1	2.39×10^8	Interior	236.3
17	490	−1	$1.25 \times 10^{9*}$		

*The specimen is not broken at the loading cycles. -The specimen surface presents charring characteristics.

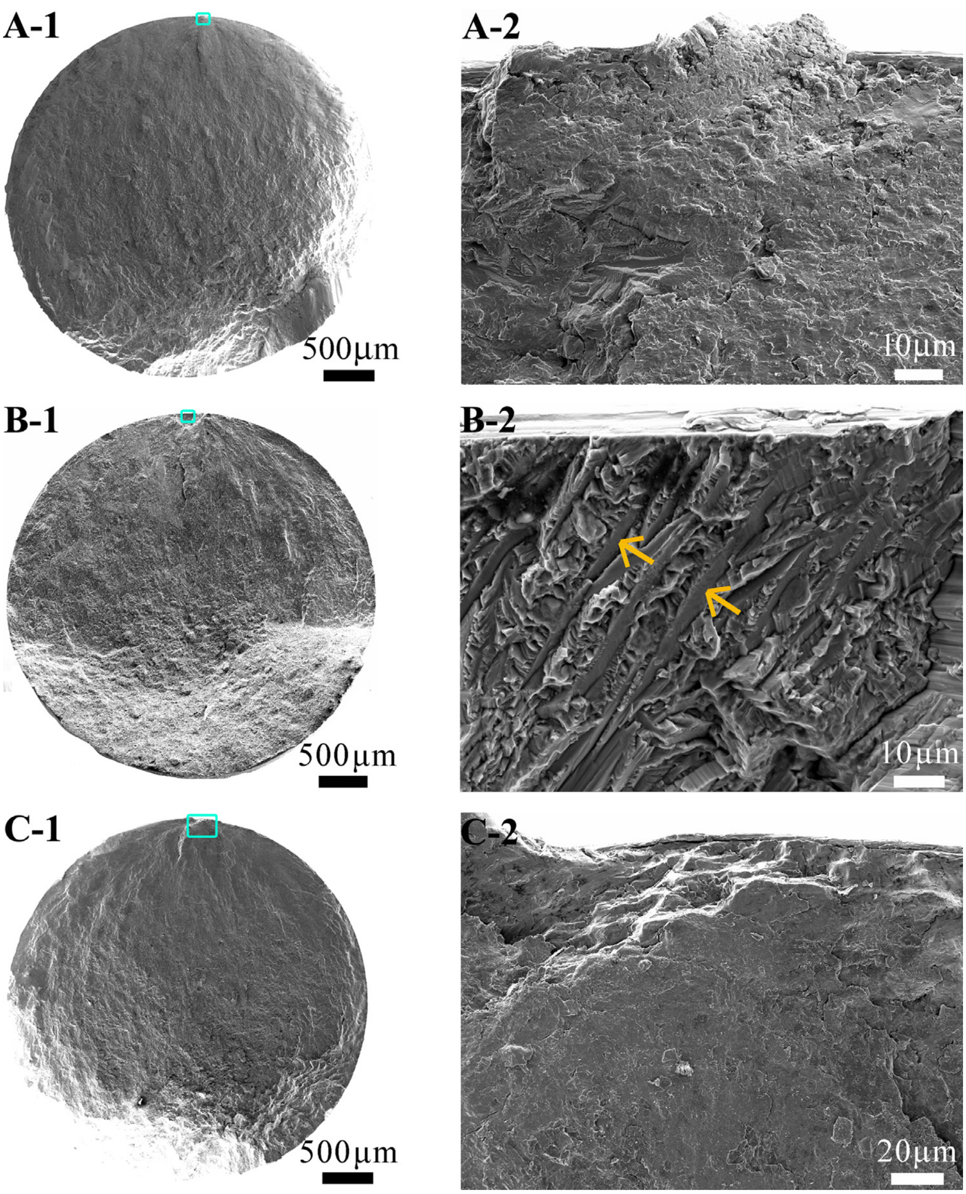

Fig. 6. Fracture surface morphology of several failed specimens under rotating bending fatigue test. A-1 and A-2: σ_a=510 MPa, N_f=1.25 × 10^5; B-1 and B-2: σ_a=489.6 MPa, N_f=7.76 × 10^6; C-1 and C-2: σ_a=484.5 MPa, N_f=1.26 × 10^8. A-1, B-1 and C-1 are SEM pictures of the whole fracture surface, respectively. A-2, B-2 and C-2 are close-ups of the rectangle regions in A-1, B-1 and C-1, respectively. The arrows in B-2 point to the regions exhibiting the facet feature.

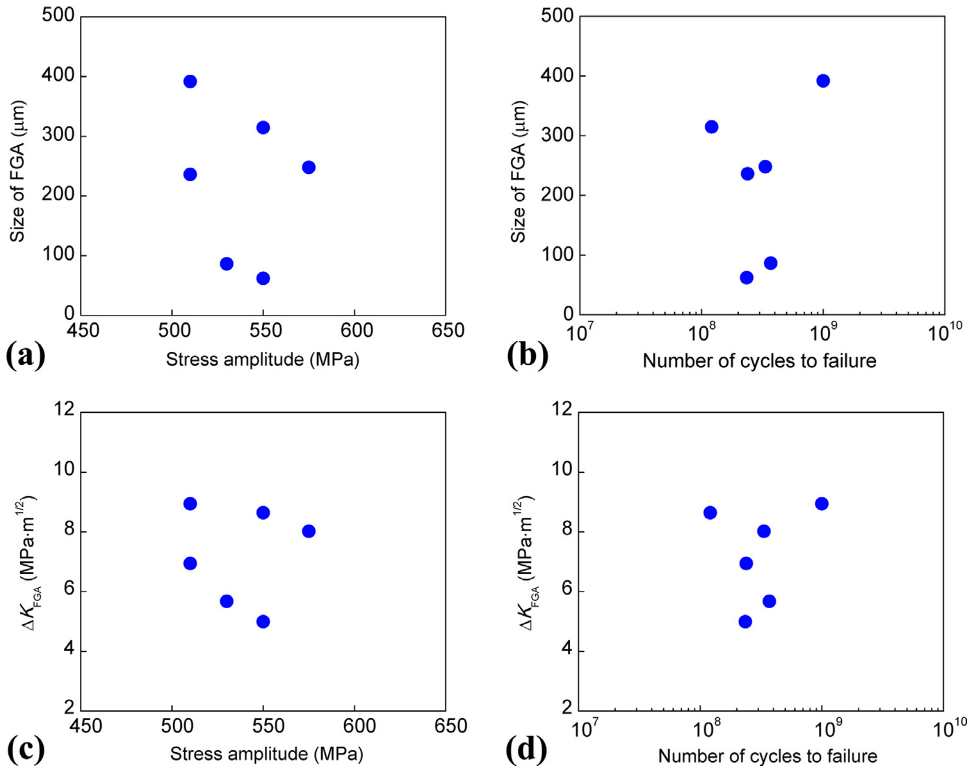

Fig. 7. Variation of FGA size with stress amplitude (a) and fatigue life (b); Variation of ΔK_{FGA} with stress amplitude (c) and fatigue life (d).

shown that the stress intensity factor range for FGA keeps almost a constant close to the threshold value of crack propagation [33-36]. Here, the FGA size is measured and the stress intensity factor range for FGA is calculated for the present AM Ti-6Al-4V. For the FGA very near to the specimen surface (B-2 in Fig. 5), it is calculated by $\Delta K_{FGA} = 0.65\sigma_a\sqrt{\pi a_{FGA}}$; while for the FGA a little far from the specimen surface (C-2 and D-2 in Fig. 5), it is calculated by $\Delta K_{FGA} = 0.5\sigma_a\sqrt{\pi a_{FGA}}$ [28,35,37]. Fig. 7 shows the variation of FGA size and the value of ΔK_{FGA} on the stress amplitude and the fatigue life. It is seen that there is no apparent variation tendency between the FGA size and the stress amplitude or the fatigue life. The value of ΔK_{FGA} varies in a range of 5.0-8.9 MPa•m$^{1/2}$. The average value is 7.2 MPa•m$^{1/2}$, which is close to the threshold value of the crack propagation 7.8 MPa•m$^{1/2}$ available for the CP Ti-6Al-4V alloy in ultra-high vacuum environment [38].

4.2. EBSD and TEM observation of extracted examples

Fig. 8 shows the EBSD results of the extracted cross-section samples along the loading direction located in C-2 in Fig. 5. It is seen from Fig. 8 that the α grains a little far beneath the fracture surface (i.e. α grains of the matrix material) are in the size of microns for all the four samples. Compared with the microstructure of the matrix material, there are much smaller grains (i.e. refined grain characteristic) in some local regions very near the fracture surface for the extracted sample 2 in FGA while the grain refinement feature is not observed very near the fracture surface for the sample 1 in FGA. For the extracted sample 3 in FGA, there seems no grain refinement. While for the extracted sample 4 in the smooth area, it suggests several smaller grains in the local region very near the fracture surface. This indicates that the refined grains do not always present for the microstructure in FGA, i.e. there are discontinuous refined grain regions for the microstructure in FGA.

The TEM observation is also used to identify the microstructure characteristics beneath the fracture surface by the consideration that the resolution of TEM is higher (the minimum resolution is ~1 nm) in comparison with the EBSD (the minimum resolution is ~10 nm). Fig. 9 shows the TEM images and SAD patterns for the extracted cross-section samples 2 and 3 located in C-2 in Fig. 5. The diameter of the SAD is 170 nm. It is seen that the patterns composed of a series of rings or diffused rings in locations I and III indicate the polycrystalline structure (i.e. many refined grains) in this selected area, while the patterns of regular dots or isolated spots in locations II, IV, VI-IX indicate a single crystal or just a few grains in this selected area. The SAD pattern is also shown for the region (location V) a little far beneath the crack surface (i.e. the matrix material). The isolated spots suggest just a few grains in this selected area. Considering that the diameter of the SAD is 170 nm, the refined grains in locations I and III are much smaller than 170 nm, i.e. the refined grains very near the fracture surface in FGA are much smaller than those of the original matrix material. Therefore, the refined grains

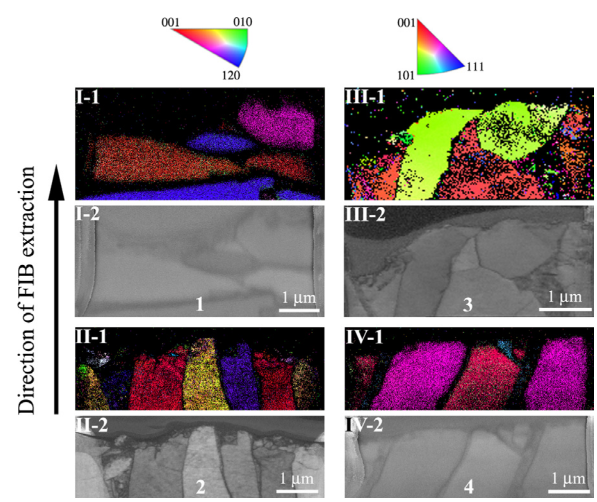

Fig. 8. EBSD results of the extracted cross-section samples 1-4 located in C-2 in Fig. 5, in which I-1, II-1, III-1 and IV-1 are the inverse pole figure maps, I-2, II-2, III-2 and IV-2 are the band contrast maps.

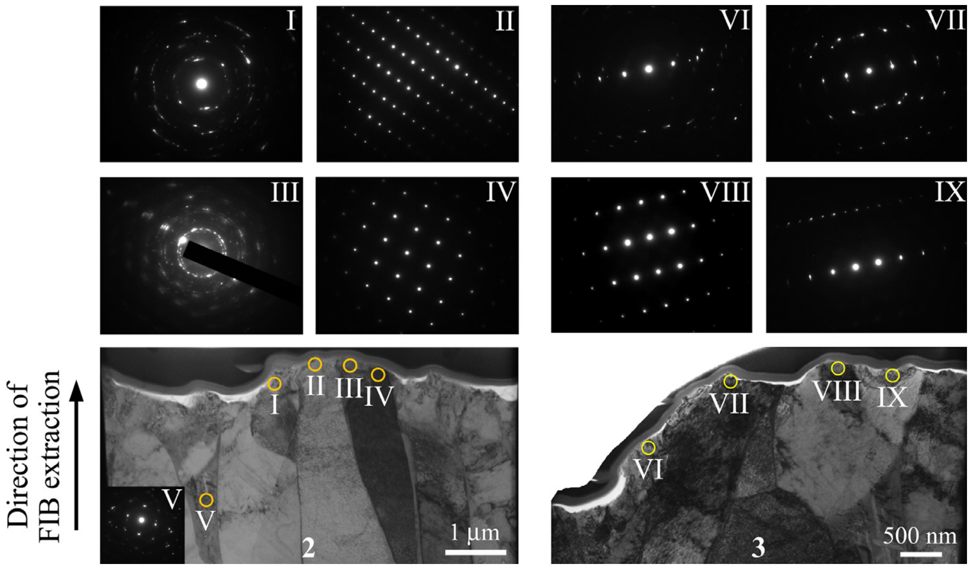

Fig. 9. TEM observations of the extracted cross-section samples 2 and 3 located in C-2 in Fig. 5, in which the circles indicate the locations where the SAD diffraction are obtained.

beneath the fracture surface in FGA should be induced by the fatigue loading in VHCF regime.

The TEM observation also indicates that the refined grain regions are discontinuous in FGA. This result is different from that observed for the FGA (rough area) of CP Ti-6Al-4V in VHCF regime, which presents a layer of nano-grains at the stress ratio R =–1 [24]. But it is similar to the observation for FGA of high strength steels in VHCF regime which exhibits the discontinuous refined grain regions [39,40].

4.3. Mechanism of crack initiation and early growth

EBSD and TEM observations indicate that the microstructure of the AM Ti-6Al-4V beneath the fracture surface in FGA exhibits the characteristic of discontinuous refined grain regions. This result is similar to that observed for high strength steels in VHCF regime, which also presents the feature of discontinuous refined grain regions beneath the fracture surface in FGA [39,40].

According to the work by Van Swam et al. [41], the microstructure evolution is related to the dislocation interaction and rearrangement during cyclic deformation, and the dislocation cell structure was observed for VHCF of a medium carbon steel, which led to the formation of small sub grains or low angle grain boundaries [42]. Moreover, the refined grains in front of the crack tip has been observed for high strength steels in VHCF regime [39,43], and no grain refinement phenomenon was observed in the vicinity of the crack tip or in the region beneath the crack surface for a martensitic stainless steel after a large number of repeating compressive loadings [40]. This indicates that the grain refinement in FGA of the AM Ti-6Al-4V is the result of dislocation interaction due to the high strain localization by microstructure inhomogeneity, deformation incompatibility or defects. Then, the cracks form within the refined grains or along the refined grain - common grain interface during the following cyclic loadings due to the decrease of threshold value for crack initiation in the regions of fine grains [44]. The cracks form within the refined grains and along the refined grain – common grain interface have been observed for high strength steels in VHCF regime [39,45].

On the other hand, the cyclic plastic deformation is highly localized in VHCF regime [46]. The fatigue crack of AM Ti-6Al-4V could at first initiate at the defects, larger α-phase, α-phase clusters or the interfaces due to the microstructure inhomogeneity and deformation incompatibility [16,23,47]. In this case, the formation of the cracks is irrespective of the grain refinement, and the microstructure in the crack surface presents no grain refinement feature. So, it is thought that, the mechanism of the crack initiation and early growth of titanium alloys in VHCF regime is attributed to the formation of grain refinement caused by the interaction between dislocations over a number of cyclic loadings followed by cracks combined with the cracks formed at defects, α-phase, interfaces, etc. during cyclic loadings, similar to that for the crack initiation and early growth of high strength steels in VHCF regime [39,40]. The model could also explain the phenomenon that the microstructure beneath the crack initiation and early growth region exhibits a layer of refined grains for CP Ti-6Al-4V in VHCF regime [24], which is a special case of the proposed mechanism that the crack initiation and early growth is due to the grain refinement followed by cracks.

5. Conclusions

In this paper, the VHCF behavior of an AM Ti-6Al-4V treated by hot-isostatic pressing is investigated by use of the ultrasonic frequency fatigue test and rotating bending fatigue test. The main results are as follows.

(1) Loading types have important influence on the fatigue behavior of the present AM Ti-6Al-4V. The fatigue crack only initiates from the specimen surface under rotating bending fatigue test, while the fatigue crack tends to initiate from the interior of the specimen in VHCF regime under ultrasonic frequency fatigue test. The fatigue performance of the present AM Ti-6Al-4V under ultrasonic frequency fatigue test is higher than that under rotating bending fatigue test.
(2) For the interior crack initiation in VHCF regime, the fracture surface presents fish-eye like pattern and FGA morphology. EBSD and TEM observations indicate that there are discontinuous refined grain regions beneath the fracture surface in FGA. The stress intensity factor range for FGA is in the range of 5.0-8.9 MPa•m$^{1/2}$, which approximates to the threshold value of crack propagation 7.8 MPa•m$^{1/2}$ for the CP Ti-6Al-4V alloy in ultra-high vacuum environment [38].
(3) The paper indicates that the mechanism of the crack initiation and early growth of titanium alloys in VHCF regime is attributed to the grain refinement caused by dislocation interaction over a number of cyclic loadings followed by cracks in combination with the cracks formed at defects, α-phase, interfaces, etc. during cyclic loadings.
(4) A comparison of the fatigue performance of the present AM Ti-6Al-4V with the CP Ti-6Al-4V indicates that the fatigue perfor-

mance of AM Ti-6Al-4V is comparable to that of the CP Ti-6Al-4V.

Declaration of Competing Interest

The authors declare that they have no known competing financial interests or personal relationships that could have appeared to influence the work reported in this paper.

CRediT authorship contribution statement

Chengqi Sun: Conceptualization, Methodology, Formal analysis, Investigation, Writing - original draft, Visualization, Writing - review & editing, Supervision. **Weiqian Chi:** Visualization, Investigation. **Wenjing Wang:** Writing - review & editing. **Yan Duan:** Resources.

Acknowledgements

The authors gratefully acknowledge the support of the National Natural Science Foundation of China Basic Science Center for "Multiscale Problems in Nonlinear Mechanics" (11988102), the National Natural Science Foundation of China (91860112) and the Strategic Priority Research Program of the Chinese Academy of Sciences (XDB22020200). The authors also thank for the great help of Professor Yujie Wei in Institute of Mechanics, Chinese Academy of Sciences in preparing the manuscript.

References

[1] Bayati P, Jahadakbar A, Barati M, Nematollahi M, Saint-Sulpice L, Haghshenas M, et al. Toward low and high cycle fatigue behavior of SLM-fabricated NiTi: considering the effect of build orientation and employing a self-heating approach. Int J Mech Sci 2020;185:105878.
[2] Hirata T, Kimura T, Nakamoto T. Effects of hot isostatic pressing and internal porosity on the performance of selective laser melted AlSi10Mg alloys. Mater Sci Eng A 2020;772:138713.
[3] Jin N, Yan Z, Wang Y, Cheng H, Zhang H. Effects of heat treatment on microstructure and mechanical properties of selective laser melted Ti-6Al-4V lattice materials. Int J Mech Sci 2021;190:106042.
[4] Drücker S, Schulze M, lpsen H, Bandegani L, Hoch H, Kluge M, Fiedler B. Experimental and numerical mechanical characterization of additively manufactured Ti6Al4V lattice structures considering progressive damage. Int J Mech Sci 2021;189:105986.
[5] Wu Z, Wu S, Zhang J, Song Z, Hu Y, Kang G, Zhang H. Defect Induced Fatigue Behaviors of Selective Laser Melted Ti-6Al-4V via Synchrotron Radiation X-Ray Tomography. Acta Metall Sin 2019;55:811–20.
[6] Zhao X, Wei QS, Song B, Liu Y, Luo XW, Wen SF, Shi YS. Fabrication and characterization of AISI 420 stainless steel using selective laser melting. Mater Manuf Process 2015;30:1283–9.
[7] Pei C, Zeng W, Yuan H. A damage evolution model based on micro-structural characteristics for an additive manufactured superalloy under monotonic and cyclic loading conditions. Int J Fatigue 2020;131:105279.
[8] Kong H, Jiang T, Liu C, Ying S, Zhao K. Study on fretting fatigue fracture of TB6 high strength titanium alloy lugs under multiaxial complex stress. Materials Reports 2020;34:14134–9 in Chinese.
[9] Xu W, Yang X, Zhong B, Guo G, Liu L, Tao C. Multiaxial fatigue investigation of titanium alloy annular discs by a vibration-based fatigue test. Int J Fatigue 2017;95:29–37.
[10] Murr LE, Quinones SA, Gaytan SM, Lopez MI, Rodela A, Martinez EY, Hernandez DH, Martinez E, Medina F, Wicker RB. Microstructure and mechanical behavior of Ti–6Al–4V produced by rapid layer manufacturing, for biomedical applications. J Mech Behav Biomed Mater 2009;2:20–32.
[11] Tridello A, Fiocchi J, Biffi CA, Chiandussi G, Rossetto M, Tuissi A, et al. VHCF response of heat-treated SLM Ti6Al4V Gaussian specimens with large loaded volume. Procedia Struct Integrity 2019;18:314–21.
[12] Shanyavskiy AA. Very-High-Cycle-Fatigue of in-service air-engine blades, compressor and turbine. Sci China Phys Mech Astron 2014;57:19–29.
[13] Edwards P, Ramulu M. Fatigue performance evaluation of selective laser melted Ti-6Al-4V. Mater Sci Eng A 2014;598:327–37.
[14] Masuo H, Tanaka Y, Morokoshi S, Yagura H, Uchida T, Yamamoto Y, et al. Effects of defects, surface roughness and HIP on fatigue strength of Ti-6Al-4V manufactured by additive manufacturing. Procedia Struct Integrity 2017;7:19–26.
[15] Greitemeier D, Palm F, Syassen F, Melz T. Fatigue performance of additive manufactured TiAl6V4 using electron and laser beam melting. Int J Fatigue 2017;94:211–17.
[16] Zuo JH, Wang ZG, Han EH. Effect of microstructure on ultra-high cycle fatigue behavior of Ti-6Al-4V. Mater Sci Eng A 2008;473:147–52.
[17] Huang ZY, Liu HQ, Wang HM, Wagner D, Khan MK, Wang QY. Effect of stress ratio on VHCF behavior for a compressor blade titanium alloy. Int J Fatigue 2016;93:232–237.
[18] Li Y, Song Q, Feng S, Sun C. Effects of loading frequency and specimen geometry on high cycle and very high cycle fatigue life of a high strength titanium alloy. Materials 2018;11:1628.
[19] Nie B, Zhao Z, Ouyang Y, Chen D, Chen H, Sun H, Liu S. Effect of low cycle fatigue predamage on very high cycle fatigue behavior of TC21 titanium alloy. Materials 2017;10:1384.
[20] Qian G, Li Y, Paolino DS, Tridello A, Berto F, Hong Y. Very-high-cycle fatigue behavior of Ti-6Al-4V manufactured by selective laser melting: Effect of build orientation. Int J Fatigue 2020;136:105628.
[21] Qian G, Jian Z, Pan X, Berto F. In-situ investigation on fatigue behaviors of Ti-6Al-4V manufactured by selective laser melting. Int J Fatigue 2020;133:105424.
[22] Wycisk E, Siddique S, Herzog D, Walther F, Emmelmann C. Fatigue performance of laser additive manufactured Ti-6Al-4V in very high cycle fatigue regime up to 109 cycles. Frontiers in Materials 2015;2:1–8.
[23] Günther J, Krewerth D, Lippmann T, Leuders S, Tröster T, Weidner A, Biermann H, Niendorf T. Fatigue life of additively manufactured Ti–6Al–4V in the very high cycle fatigue regime. Int J Fatigue 2017;94:236–45.
[24] Su H, Liu X, Sun C, Hong Y. Nanograin layer formation at crack initiation region for very-high-cycle fatigue of a Ti–6Al–4V alloy. Fatigue Fract Eng Mater Struct 2017;40:979–93.
[25] Takeuchi E, Furuya Y, Nagashima N, Matsuoka S. The effect of frequency on the giga-cycle fatigue properties of a Ti-6Al-4V alloy. Fatigue Fract Eng Mater Struct 2008;31:599–605.
[26] Liu X, Sun C, Hong Y. Effects of stress ratio on high-cycle and very-high-cycle fatigue behavior of a Ti–6Al–4V alloy. Mater Sci Eng A 2015;622:228–35.
[27] Heinz S, Balle F, Wagner G, Eifler D. Analysis of fatigue properties and failure mechanisms of Ti6Al4V in the very high cycle fatigue regime using ultrasonic technology and 3D laser scanning vibrometry. Ultrasonics 2013;53:1433–40.
[28] Murakami Y. Metal Fatigue: Effects of Small Defects and Nonmetallic Inclusions. Oxford: Elsevier Science; 2002.
[29] Szczepanski CJ, Jha SK, Larsen JM, Jones JW. Microstructural influences on very high cycle fatigue crack initiation in Ti-6246. Metall Mater Trans A 2008;39:2841–51.
[30] Everaerts J, Verlinden B, Wevers M. Investigation of fatigue crack initiation facets in Ti-6Al-4V using focused ion beam milling and electron backscatter diffraction. J Microsc-Oxford 2017;267:57–69.
[31] Song Q, Li Y, Wang L, Huang R, Sun C. Effect of rise and fall time on dwell fatigue behavior of a high strength titanium alloy. Metals 2019;9:914.
[32] Sun C, Li Y, Huang R, Wang L, Liu J, Zhou L, Duan G. Crack initiation mechanism and fatigue life of titanium alloy Ti–6Al–2Sn–2Zr–3Mo-X: Effects of stress ratio and loading frequency. Mater Sci Eng A 2020;798:140265.
[33] Sakai T, Sato Y, Oguma N. Characteristic S–N properties of high-carbon-chromium-bearing steel under axial loading in long-life fatigue. Fatigue Fract Eng Mater Struct 2002;25:765–73.
[34] Zhao A, Xie J, Sun C, Lei Z, Hong Y. Prediction of threshold value for FGA formation. Mater Sci Eng A 2011;528:6872–7.
[35] Sun C, Liu X, Hong Y. A two-parameter model to predict fatigue life of high-strength steels in a very high cycle fatigue regime. Acta Mech Sin 2015;31:383–91.
[36] Sun C, Song Q, Zhou L, Pan X. Characteristic of interior crack initiation and early growth for high cycle and very high cycle fatigue of a martensitic stainless steel. Mater Sci Eng A 2019;758:112–20.
[37] Shiozawa K, Lu L, Ishihara S. S–N curve characteristics and subsurface crack initiation behaviour in ultra-long life fatigue of a high carbon–chromium bearing steel. Fatigue Fract Eng Mater Struct 2001;24:781–90.
[38] Oguma H, Nakamura T. Fatigue crack propagation properties of Ti-6Al-4V in vacuum environments. Int J Fatigue 2013;50:89–93.
[39] Sun C, Song Q, Zhou Liu J, Wang Y, Wu X, Wei Y. The formation of discontinuous gradient regimes during crack initiation in high strength steels under very high cycle fatigue. Int J Fatigue 2019;124:483–92.
[40] Song Q, Sun C. Mechanism of crack initiation and early growth of high strength steels in very high cycle fatigue regime. Mater Sci Eng A 2020;771:138648.
[41] Van Swam LF, Pelloux RM. Fatigue behavior of maraging steel 300. Metall Trans A 1975;6:45–54.
[42] Koster M, Wagner G, Eifler D. Cyclic deformation behavior of a medium carbon steel in the VHCF regime. Procedia Eng 2010;2:2189–97.
[43] Spriestersbach D., Grad P., Brodyanski A., Lösch J., Kopnarski M., Kerscher E. Very high cycle fatigue crack initiation: investigation of fatigue mechanisms and threshold values for 100Cr6. Christ H-J (Ed.), Fatigue of Materials at Very High Numbers of Loading Cycles. 2018, p.167–210.
[44] Niendorf T, Rubitschek F, Maier HJ, Canadine D, Karaman I. On the fatigue crack growth–microstructure relationship in ultrafine-grained interstitial-free steel. J Mater Sci 2010;45:4813–21.
[45] Tofique MW, Bergström J, Svensson K. Very high cycle fatigue of cold rolled stainless steels, crack initiation and formation of the fine granular area. Int J Fatigue 2017;100:238–50.
[46] Chai G, Zhou N, Ciurea S, Andersson M, Peng RL. Local plasticity exhaustion in a very high cycle fatigue regime. Scr Mater 2012;66:769–72.
[47] Szczepanski CJ, Jha SK, Larsen JM, Jones JW. Microstructural influences on very high cycle fatigue crack initiation in Ti-6246. Metall Mater Trans A 2008;39:2841–51.